PROCEEDINGS OF SCIENCE

# Calibration of the ASTRI-1 Cherenkov camera

**Davide Mollica,[a,*] Osvaldo Catalano,[a] Giovanni Contino,[a] Milvia Capalbi,[b] Mattia Corpora,[a] Fabio Paolo Lo Gerfo,[a] Pierluca Sangiorgi,[a] Giuseppe Sottile,[a] Giuseppe Leto,[c] Teresa Mineo,[a] Salvatore Scuderi,[d] Gino Tosti[e] and Giovanni Pareschi[f] for the ASTRI Project**

[a] *INAF, Istituto di Astrofisica Spaziale e Fisica Cosmica, Via Ugo la Malfa 153, I-90146 Palermo, Italy*
[b] *INAF - Osservatorio Astronomico di Roma, Via Frascati 33, I-00078 Monte Porzio Catone, Italy*
[c] *INAF, Osservatorio Astronomico di Catania, Via Santa Sofia 78, I-95123 Catania, Italy*
[d] *INAF, Istituto di Astrofisica Spaziale e Fisica Cosmica, Via Alfonso Corti 12, I-20133 Milano, Italy*
[e] *Dipartimento di Fisica, Università degli Studi di Perugia, I-06123 Perugia, Italy*
[f] *INAF, Osservatorio Astronomico di Brera, Via Brera 28, I-20121 Milano, Italy*

*E-mail:* davide.mollica@inaf.it

The ASTRI project, led by the Italian National Institute for Astrophysics (INAF), aims to deploy an array of nine small-sized (4-m diameter) Imaging Atmospheric Cherenkov Telescopes at the Teide Observatory in Tenerife. The system will study astronomical sources emitting in the very high-energy range above 1 TeV up to 200 TeV. Each telescope is equipped with a Cherenkov camera based upon Silicon Photo-Multiplier (SiPM) sensors. The focal plane is composed of 2368 pixels arranged in 37 Photon Detection Modules (PDMs) of 8×8 pixels covering a field of view of about 10.5 degree. The camera electronics is based on a peak detection circuit and is designed to perform self-trigger of the whole focal plane in order to detect and digitize Cherenkov signals while minimizing the data transfer volume. One of the nine telescopes (ASTRI-1) is already in its commissioning phase, collecting data since September 2024 when the first industrial version of the ASTRI Cherenkov camera was mounted on the telescope. In this contribution we report on the camera calibration carried out at the beginning of the commissioning phase and on the system stability monitoring through on-site daily calibration runs. All the calibrations have been performed with the camera internal calibration system that allows the on-site extraction of the optimal camera configuration parameters and of the calibration coefficients needed for the data analysis.

39th International Cosmic Ray Conference (ICRC2025)
15–24 July 2025
Geneva, Switzerland


*Speaker





PoS(ICRC2025)768

## 1. Introduction

The ASTRI Mini-Array [1, 2] is designed to study astronomical sources emitting at very high-energy (VHE) in the 1 TeV-200 TeV energy band. The array will consist of nine small-sized (4-m diameter) and large field of view (10.5°) Imaging Atmospheric Cherenkov Telescopes (IACTs) under deployment at the *Observatorio del Teide* (Tenerife, Spain). The array telescopes have a dual-mirror Schwarzschild-Couder optical design characterized by a small plate-scale (about 37.5 mm/deg) that allows for the use of Silicon Photo-Multiplier (SiPM) detectors. Currently, one of the nine telescopes, ASTRI-1, is in its commissioning phase, collecting data since September 2024 [3] following the installation of the first industrial version of the ASTRI Cherenkov camera. A second telescope, ASTRI-3, is about to be completed.

This contribution details the key calibration results for the ASTRI-1 Cherenkov camera. These measurements have been performed on-site, by means of the camera internal calibration system, at the beginning of the commissioning phase and during regular data taking. Only a short overview of the focal plane design and of the signal acquisition and processing system is provided here. A detailed description of the camera architecture can be found in [4].

### 1.1 The ASTRI Cherenkov Camera

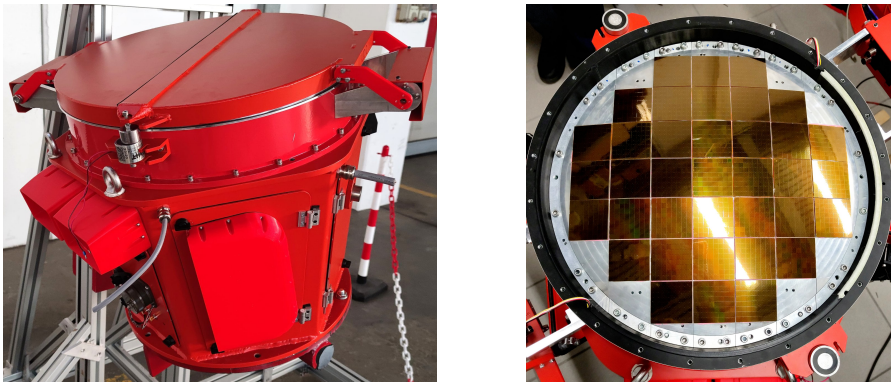

**Figure 1:** The ASTRI-1 Cherenkov camera during the assembly phase. Left) Camera body view with the lids closed. Right) Camera focal plane view with all the 37 PDMs mounted, SiPM tiles were still covered by a kapton protective film.

The focal plane of the ASTRI Mini-Array camera is composed of 37 Photon Detection Modules (PDMs). Each PDM contains a Hamamatsu S14521 SiPM tile, the Front-End Electronics (FEE), and a Field Programmable Gate Array (FPGA). The SiPM tile is an 8×8 array of 7×7 $mm^2$ pixels, resulting in a focal plane populated by 2368 pixels. The camera body and focal plane are shown in Figure 1. The camera has 12 thermoelectric coolers that keep the focal plane structure temperature at $(15 \pm 1)\,^{\circ}C$. Each PDM has three temperature sensors allowing a continuous monitoring of the thermal conditions of the focal plane. The temperature data are used to dynamically adjusts the bias voltage of the SiPMs in order to ensure a stable detector response under varying environmental conditions.

Signals from SiPMs are processed by the FEE, whose architecture utilizes two 32-channel CITIROC-1A [5] Application-Specific Integrated Circuits (ASICs). Each channel within these

ASICs is split into three signal processing lines: a trigger chain, a High-Gain (HG) acquisition chain, and a Low-Gain (LG) acquisition chain. The HG and LG acquisition chains have distinct gain configurations, with a nominal gain-ratio of 20, and are shaped with the same programmable shaping time, nominally 25 ns. Each acquisition chain is equipped with a peak-detection circuit which measures the maximum amplitude of the shaped signal. The trigger chain operates at the same gain level of the HG chain. It is, however, connected to a faster shaper, with 15 ns shaping time, and subsequently to a discriminator. This discriminator employs a 10-bit programmable threshold, common to all 32 channels of a given ASIC, to generate a pixel trigger signal. The reference voltage of each channel can be fine-tuned by a 4 bit Digital-to-Analog Converter (DAC).

A Xilinx Artix 7 FPGA handles the generation of a *PDM trigger* when $n$ contiguous pixels exceed the selected threshold. This PDM trigger is subsequently sent to the back-end electronics, which, in turn, sends back a *camera trigger* signal to all PDMs. Then the peak detector is enabled and, after a programmable delay, the signal peak value for both HG and LG chains is digitised.

## 2. On-site calibration procedures

The on-site calibration of the camera is a critical process that aims to ensure optimal and uniform performance across the entire focal plane. The following subsections describe the results of the application of the key procedures developed for this purpose, which include the determination of the SiPMs breakdown voltage and the characterization of its temperature dependence, the alignment of the trigger thresholds for all ASICs channels, and the gain calibration needed to convert from analog-to-digital units to photo-electron (pe). These methods are designed to be performed efficiently on-site using the camera internal calibration system. For a comprehensive description of these procedures refer to [6].

### 2.1 Breakdown voltage

The first camera calibration step involves measuring SiPMs breakdown voltage, $V_{\mathrm{br}}$, in order to determine the operational voltage, $V_{\mathrm{op}}$, to be applied. We have developed an innovative method that allows this procedure to be performed on-site using the camera internal calibration system. This method is based on measuring signal variance as a function of bias voltage while illuminating the focal plane with a stable continuous light source. Assuming a Borel distribution for cross-talk discharges, the breakdown voltage of each pixel can be extracted with the following model:

$$\sigma^2\left(V_{\mathrm{op}}\right) = \begin{cases} \sigma_0^2 & \text{if } V_{\mathrm{op}} < V_{\mathrm{br}}, \\ \sigma_0^2 + \beta \dfrac{V_{\mathrm{ov}}^2\left(1 - \mathrm{e}^{-\frac{V_{\mathrm{ov}}}{\alpha}}\right)}{\left(1 - \gamma V_{\mathrm{ov}}\left(1 - \mathrm{e}^{-\frac{V_{\mathrm{ov}}}{\alpha}}\right)\right)^3} & \text{if } V_{\mathrm{op}} > V_{\mathrm{br}}, \end{cases} \tag{1}$$

where:

- $V_{\mathrm{ov}} = V_{\mathrm{op}} - V_{\mathrm{br}}$ is the the *over-voltage*;
- $\sigma_0^2$ is the signal variance due to leakage current and electronic noise;
- $\beta$ is a proportionality factor that depends on the readout electronics, micro-cells capacitance and light source intensity;

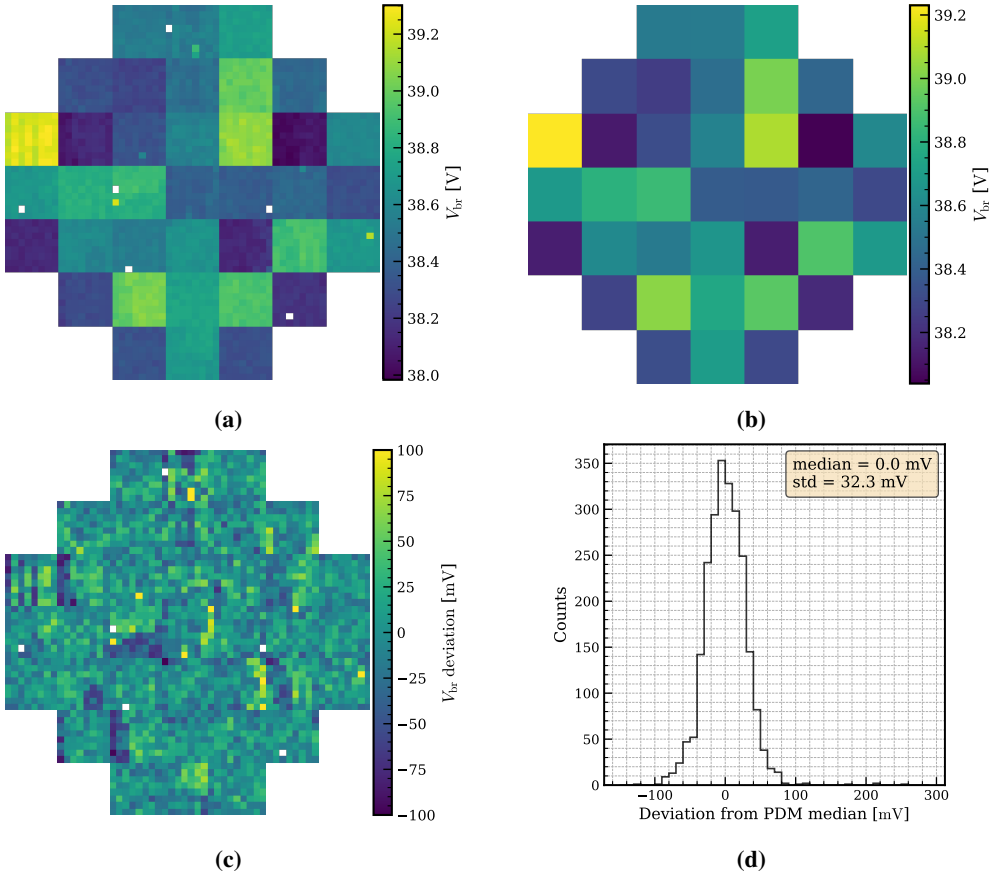


**Figure 2:** a) Measured $V_{br}$ of all pixels. b) Median $V_{br}$ of each module. c) $V_{br}$ deviation from the PDM median. d) Distribution of the $V_{br}$ deviation from the PDM median.

- $\gamma$ describes the linear relation between $V_{ov}$ and the number of discharge-induced photons that can generate a cross-talk discharge;
- $\alpha$ describes how fast the breakdown probability raises with the over-voltage.

The $V_{br}$ measurement results are shown in figure 2a. Since the $V_{op}$ is shared by all 64 pixels of each PDM, we select as reference $V_{br}$ the median of the values measured for each PDM, as shown in figure 2b. Figures 2c and 2d show the deviation from the PDM median value, which has a null median and a dispersion of 32.3 mV. Considering the $V_{ov}$ dependence of the Photon-Detection Efficiency (PDE), reported in [7], this translates into an absolute PDE dispersion of 0.2 % (that is a relative dispersion of 4 ‰) in the 450 nm to 470 nm spectral range.

### 2.1.1 Temperature compensation

The aforementioned measurement has been carried out with the thermal control system set to the nominal 15 °C target temperature. In order to take into account temperature fluctuations throughout the whole focal plane, the operational voltage of each PDM is adjusted to compensate for the temperature-induced $V_{br}$ shift:

$$V_{op}(T) = V_{br,0} + (T - T_0)\,\frac{dV_{br}}{dT} + V_{ov}. \tag{2}$$

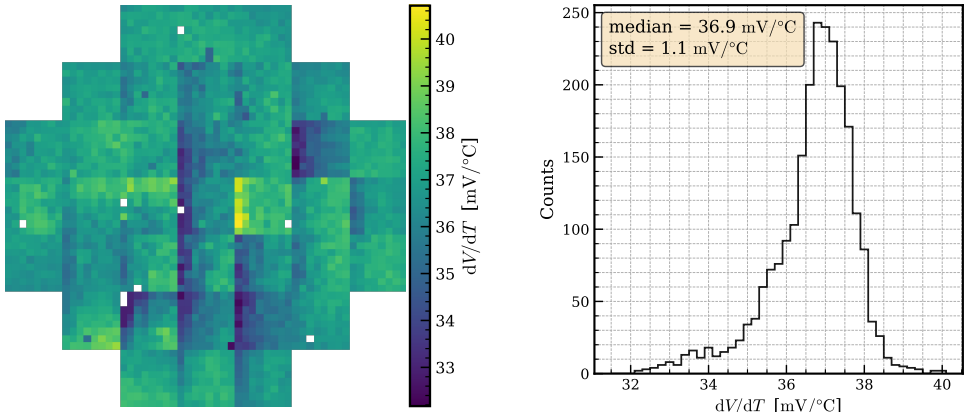


**(a)** **(b)**

**Figure 3:** Measured SiPM $V_{\mathrm{br}}$ temperature dependence $\mathrm{d}V_{\mathrm{br}}/\mathrm{d}T$: a) focal plane image; b) pixel values distribution.

In this way, the over-voltage is kept constant and so are PDE, gain and cross-talk. The reference temperature $T_0$ is the temperature registered by a PDM during the breakdown voltage measurement at the nominal target temperature. In order to measure $\mathrm{d}V_{\mathrm{br}}/\mathrm{d}T$, the $V_{\mathrm{br}}$ has been also measured setting the target temperature to 10 °C and 20 °C. The linear fit results of the $V_{\mathrm{br}} - T$ relation for each pixel are shown in figure 3a and 3b. The median value is about 37 mV/°C. Non-uniformities are under investigation, however, during typical operations, they are not likely to affect the overall camera response in a substantial way.

## 2.2 Trigger channel alignment

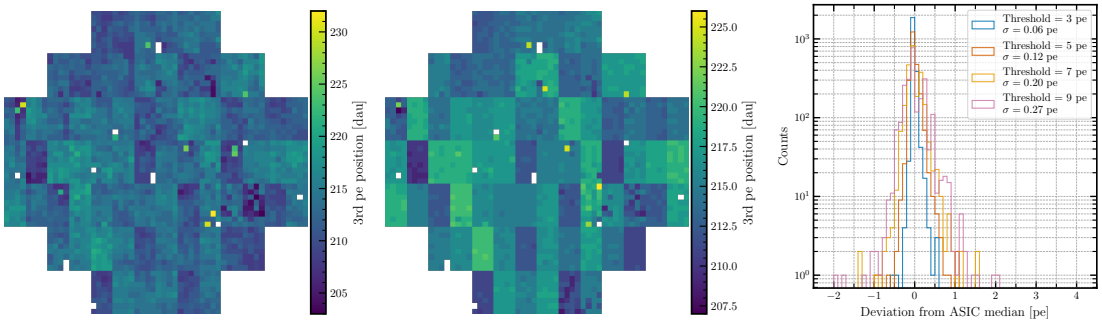


**(a)** **(b)** **(c)**

**Figure 4:** a) Third photo-electron threshold before the alignment. b) Third photo-electron threshold after the alignment. b) Expected pixel threshold dispersion at different camera threshold.

The next calibration step consists of aligning the trigger signals. As previously mentioned, differences in pixel gain are expected due to the common operational voltage. Moreover, channel-to-channel variations of gain and discriminator reference voltage are also expected. All 32 channels of the Citiroc-1A ASIC have a shared threshold, programmable by a 10-bit Digital-to-Analog Converter (DAC), therefore it is necessary to equalize trigger channels of each ASIC. To compensate for these

channel-to-channel variations, any misalignment can be corrected by means of a programmable 4-bit DAC that adjusts the discriminator reference voltage for each channel individually.

The optimal adjustment for each channel was determined by analysing its *staircase curve* (dark-count rate as a function of threshold) and minimizing the number of unaligned pixels per ASIC. This procedure allowed us to align the trigger signals up to the third photo-electron. The corresponding threshold of each pixel before and after the alignment is shown in figures 4a and 4b, respectively. The aligned staircase curves are used to extract the coefficients needed to convert from the global photo-electron threshold to the corresponding 10-bit DAC value for each ASIC. Due to the inherent gain differences, the threshold misalignment is expected to increase at higher threshold levels. However, as shown in Figure 4c, the trigger signals remain well-aligned even at a threshold of 7 pe, a typical setting for low-zenith angle observations without moonlight [3], with a residual misalignment of about 0.2 pe.

### 2.3 Gain calibration

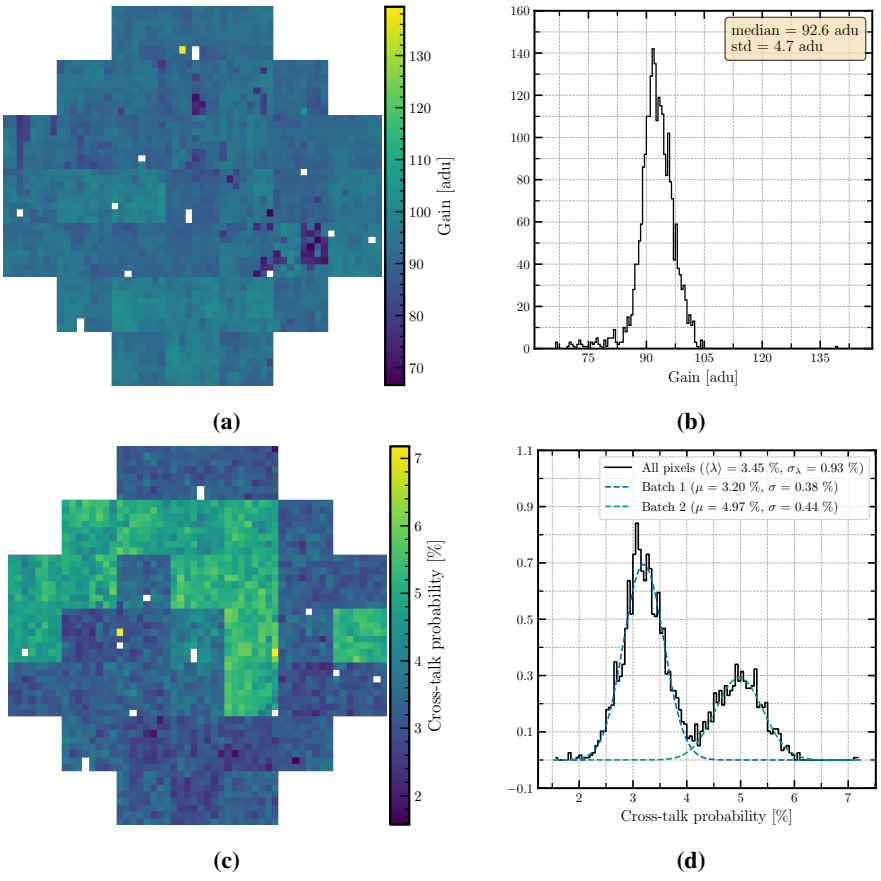


**Figure 5:** a) Measured gain across the camera. b) Measured gain distribution. c) Measured cross-talk across the camera. d) Measured cross-talk distribution.

SiPM gain and cross-talk are obtained from Pulse-Height Distribution (PHD). The PHD of each SiPM is recorded illuminating the focal plane with blue light flashes with a pulse duration of 10 ns and at a constant frequency of 1000 Hz. The resulting distribution is well described by a

Gaussian-smeared generalized Poisson distribution [8]

$$f_{\mathrm{PHD}}(x) = \sum_{k=0}^{\infty} f_{\mathrm{G}}\left(x,\ x_{\mathrm{ped}} + k\bar{g},\ \sqrt{\sigma^2_{\mathrm{ped}} + k\sigma^2_{\mu\mathrm{cells}}}\right) p_{\mathrm{GP}}(k, \mu, \lambda), \tag{3}$$

where:

- $f_{\mathrm{G}}(x, \mu, \sigma)$ is a normal probability density function with mean $\mu$ and standard deviation $\sigma$;
- $p_{\mathrm{GP}}$ is the probability mass function of a compound Poisson sum of Borel cross-talk discharges;
- $x_{\mathrm{ped}}$ and $\sigma_{\mathrm{ped}}$ are the pedestal position and dispersion (the electronic noise);
- $\bar{g}$ is the *equivalent photo-electron* (the pixel micro-cells mean gain);
- $\lambda$ is he mean number of Geiger discharges per photo-detection induced by cross-talk;
- $\sigma_{\mu\mathrm{cells}}$ is the photo-electron dispersion due to gain differences between pixel micro-cells.

The analysis results show a gain uniformity of about 5 %. The measured gain across the camera and its distribution can be seen in figures 5a and 5b respectively. The measured cross-talk shows a different mean value for 12 out of 37 PDMs, as shown in figure 5c. These probably came from different production batches. The cross-talk distribution is shown in figure 5c. The two batches are clearly distinguishable with a mean cross-talk level of 3.2 % and 5 % and a dispersion of 0.4 %.

A total of 14 pixels (white pixels in figure 5a) out of 2368 are too noisy to be reconstructed properly (or at all) and have therefore been marked as *unreliable*.

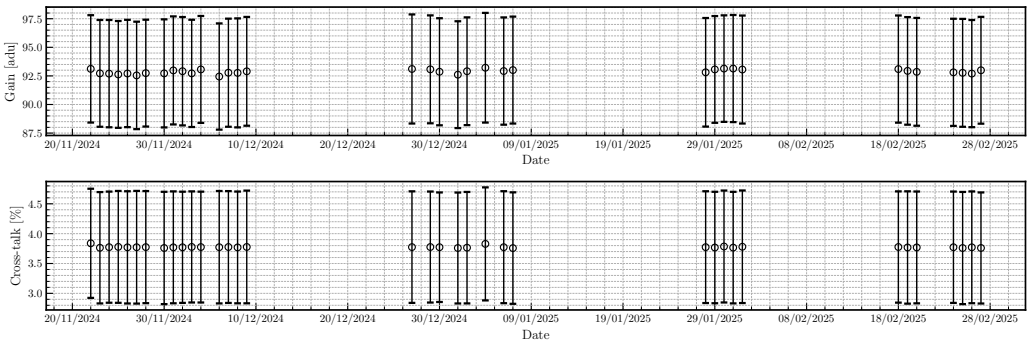


**Figure 6:** Results of the on-site monitoring of gain and cross-talk from November 2024 to February 2025. Markers indicate the mean value, and error bars represent the dispersion across the entire camera.

**Stability** Gain calibration runs are taken regularly before observations to monitor the system stability. As shown in Figure 6, the results for gain and cross-talk confirm the long-term stability and uniformity of the system response.

The mean gain shows a relative dispersion of about 0.2 % and the mean cross-talk relative dispersion is about 0.4 %. The results for individual pixels show an higher dispersion of about 0.3 % and 7 % respectively. The cross-talk measurement error is inherently high, since it depends on the relative height of PHD peaks, which can be distorted by the electronics chain.

## 3. Conclusions

We have reported on the application of the main calibration procedures, detailed in [6] , on the ASTRI-1 Cherenkov camera using its internal calibration system. These procedures have been

implemented in the ASTRI calibration software package `astricaltools` [9]. Gain calibration runs, periodically taken on-site, are automatically analysed offline the day after the observation. They are used to monitor the system stability and are passed to and used by the scientifical data reduction and analysis pipeline [10, 11] to ensure a proper data calibration.

The results of the calibration show, for the whole 10.5° focal plane, a gain uniformity of 4 % and a trigger threshold uniformity of about 2 % for conditions typical of low-zenith angle observations without moonlight. In addition, SiPM prompt cross-talk measurement performed on-site are in agreement with lab measurements [7].

These methods will be applied also to the ASTRI-3 camera, which will be completed in the next months.

## Acknowledgments

This work was conducted in the context of the ASTRI Project. We gratefully acknowledge support from the people, agencies, and organisations listed here: http://www.astri.inaf.it/en/library/. This paper went through the internal ASTRI review process.

## References

[1] S. Scuderi et al., *The ASTRI Mini-Array of Cherenkov telescopes at the Observatorio del Teide*, *Journal of High Energy Astrophysics* **35** (2022) 52.

[2] G. Pareschi, *Status of the ASTRI Mini-Array Gamma-Ray Experiment*, in *39th International Cosmic Ray Conference*, July, 2025.

[3] S. Crestan et al., *ASTRI-1: Early data and Performance*, in *39th International Cosmic Ray Conference*, July, 2025.

[4] G. Sottile et al., *The ASTRI Cherenkov Camera: from the Prototype to the Industrial Version for the Mini-Array*, in *2022 IEEE Nuclear Science Symposium and Medical Imaging Conference (NSS/MIC)*, pp. 1–5, 2022, DOI.

[5] J. Fleury et al., *Petiroc and Citiroc: front-end ASICs for SiPM read-out and ToF applications*, *JINST* **9** (2014) C01049.

[6] D. Mollica et al., *Calibration strategy of the ASTRI Mini-Array Cherenkov cameras*, *PoS* **ICRC2023** (2023) 765.

[7] G. Romeo et al., *Novel silicon photomultipliers suitable for dual-mirror small-sized telescopes of the cherenkov telescope array*, *Nuclear Instruments and Methods in Physics Research Section A: Accelerators, Spectrometers, Detectors and Associated Equipment* **908** (2018) 117–127.

[8] V. Chmill et al., *On the characterisation of SiPMs from pulse-height spectra*, *Nuclear Instruments and Methods in Physics Research Section A: Accelerators, Spectrometers, Detectors and Associated Equipment* **854** (2017) 70.

[9] D. Mollica et al., *The ASTRI Mini-Array calibration software*, in *39th International Cosmic Ray Conference*, July, 2025.

[10] S. Lombardi, F. Lucarelli, C. Bigongiari, S. Gallozzi, M. Cardillo, M. Mastropietro et al., *The data processing, simulation, and archive systems of the ASTRI Mini-Array project*, in *Software and Cyberinfrastructure for Astronomy VII*, vol. 12189 of *Society of Photo-Optical Instrumentation Engineers (SPIE) Conference Series*, p. 121890P, Aug., 2022, DOI.

[11] F. Lucarelli et al., *The Data Handling System of the ASTRI Mini-Array Project*, in *39th International Cosmic Ray Conference*, July, 2025.